3D tomographic reconstruction of light emission density of plasma in the PROTO-SPHERA experiment

Annamaria Pau[a], Shayesteh Naghinajad[a], Franco Alladio[b], Paolo Micozzi[c], Luca Boncagni[c]

[a] *Department of Structural and Geotchnical Engineering, Sapienza University of Rome, via Eudossiana 18, 00184 Roma, Italy*
[b] *INAF-IAPS National Institute of Astrophysics, Via del Fosso del Cavaliere 100, 00133 Roma, Italy*
[c] *Nuclear Research Department, ENEA Italian National Agency for Technology, Energy and Sustainable Economic Development Via Enrico Fermi 45, 00044 Frascati (RM), Italy*

Abstract

We apply a method for the reconstruction of 3D density functions based on the formulation of a corollary of the 3D Fourier slice theorem. This corollary, which we state and prove in its general case, connects projections of a 3D density function onto planes to the 3D Fourier transform of the density function itself. By applying a suitable coordinate transformation and computing the 3D inverse Fourier transform of the 2D Fourier transforms of the projections, we directly solve the inverse problem consisting in the reconstruction of a density function based on the knowledge of its projection. This method is employed to represent the visible light emission density distribution of magnetically confined plasma, using experimental data recorded by ENEA (Italian National Agency for Technology, Energy and Sustainable Economic Development) within the ambit of the PROTO-SPHERA experiment. The light emission from Helium and Hydrogen plasma is captured by multiple cam-eras arranged in cylindrical symmetry as part of an ongoing plasma physics experiment. The developed technique enabled observation of the mechanism of self-organization of a plasma torus around a centerpost, which confirmed

Email addresses: `annamaria.pau@uniroma1.it` (Annamaria Pau), `shayesteh.naghinajad94@gmail.com` (Shayesteh Naghinajad), `franco.alladio@protosphera.it` (Franco Alladio), `paolo.micozzi@enea.it` (Paolo Micozzi), `luca.boncagni@enea.it` (Luca Boncagni)

theoretical predictions. It further enabled visualization of cross-sections of plasma, and to disclose its inner organization and emission spectrum as well.

Keywords: 3D image reconstruction, magnetically confined plasma, nuclear fusion, monitoring

---

1. Introduction

Tomographic computed (CT) imaging or scanning is a technique of data treatment which enables visualization of the inner part of objects instead of making real cuts. This has obvious and important applications in the medical field, as well as in the nondestructive monitoring of structures and industrial processes. CT requires the solution of an inverse problem, which can be formulated as follows: given the knowledge of some data called projections, reconstruct the spatial distribution of a density function $f(x, y, x)$ which represents some property (for instance mass density) of an object in the 3D space. Projections are obtained by illuminating the object with stimuli which produce a measurable response, which is measured on the object boundary. Projections are, in practice, a sort of shade that the function $f(x, y, x)$ projects onto lines, or planes. The mathematical demonstration that a density function could be reproduced from an infinite set of its projections was provided by the mathematician J. Radon [29] at the beginning of last century. However, it is quite remarkable that reconstruction of images from projections was not attempted until 1940. In 1972, Hounsfield [18] proposed the first method that allowed to image plane slices of the internal structure of a human body using X-rays projections. The Nobel prize in physiology and medicine in 1979 awarded to Hounsfield and Cormack [6] for their work on the initial computed tomography device signifies the importance that this technique has in the medical field. Since then, the use of computed tomography was extended to a wide number of industrial applications [8], among which food industry [30], materials science [25], and geosciences [5].

Medical and industrial computed tomography is based on the same underlying principles but differs in the acquisition system layout, as well as in the stimulus that is used to obtain the projections, which is X-rays in medical CT, but can also be another physical source. In fact, the reflected or transmitted signal of any source which produces a measurable response of the scanned object can be used. The feasibility of using ultrasounds [21, 19, 22], the photo elastic effect [35], or even ground-penetrating radar emitting microwaves [1] has been proved to be effective to visualize internal patterns of objects. Different sources interact with different properties, which can include, besides mass density, electrical, acoustic, and electromagnetic properties of materials and tissues. For instance, in nuclear medicine, the interest is focused on reconstructing a cross-sectional image of radioactive isotope distributions within the human body [10], while in magnetic resonance the magnetic properties of the object is reconstructed [13]. The photelastic effect instead was used to determine the plane stress distribution in an optical fiber [27]. The main difference between the mentioned sources is that some of them are non-diffracting, like X-rays, which travel in straight lines [3], while some others are diffracting, like ultrasounds, that is, they are scattered in all directions, resulting in a more complex inverse problem [20].

To convert the measured response data into an image, appropriate processing is necessary. The most popular algorithms that are in use can be classified into two major categories, which are iterative and analytical methods [17]. Iterative reconstruction algorithms employ a model to predict the measured data from an initial estimate and then refine the image estimate to better fit the measured data. This process is repeated iteratively until the image quality meets a predetermined standard or until further iterations do not significantly change the image [31, 32]. Starting from the Algebraic Reconstruction Technique (ART) [15], research continues to evolve with refinements and developments, such as the customized Simultaneous Algebraic Reconstruction Technique (SART) [11], and the Simultaneous Iterative Reconstruction Technique (SIRT) [36]. Analytical algorithms are based on mathematical models and explicit formulas that directly compute the image from the acquired projection data. They can be further cathegorized into two groups: the direct or Fourier-Transform-based methods [37, 16] and the Back-Projection-based algorithms, like Simple Back Projection (SBP), Linear Back Projection (LBP) and Filtered Back Projection (FBP) [26, 36]. Fourier-Transform-based algorithms rely on the relationship between the Fourier transform of the image and the Fourier transform of its projections. More specifically, projections are obtained using Radon transforms [20], that is by computing line integrals of the density function. A more detailed discussion of the literature on the classification of CT algorithms is beyond the scope of this paper. The interested reader can consult [22, 9] for a more eshaustive presentation of the matter.

Traditionally, and up to the present day [24, 12], CT 3D scans have been obtained by assembling a stack of 2D images. In the classical tomographic approach, the 3D image is reconstructed by assembling slices of images deriving from a 2D setting of the problem of image reconstruction on several parallel planes. To do so, the Fourier slice theorem in 2D is employed, which connects the Fourier transform of the Radon transform to the 2D Fourier transform of the image itself. Despite a nth-dimension formulation of the Radon transform was provided by Radon himself, to the best of our knowledge, applications of the 3D Radon transfom are limited in the literature. In most of the cases, for the analytical reconstruction, the 3D Fourier slice theorem [4] is applied in the form connecting 1D Fourier transforms of line subsets of the 3D Radon transform [34, 38, 33], with applications also to image-recognition problems [7]. The sole reference that can be found in the literature employing the connection between 2D Fourier transforms of plane projections with central slices of the 3D Fourier volume, is the work by Zosso et al. [38], where the necessary corollary is formulated and the resulting method is employed to track bone movements in stereoscopic X-ray image series of a knee joint.

Here, we employ the imaging technique based on the corollary to Fourier slice theorem in 3D formulated by [38], but demonstrate it for the more general case of arbitrary angles. By calculating 3D inverse Fourier transforms of 2D Fourier transforms of plane projections, the 3D image of the scanned object can be reconstructed. This technique is fairly general and applies to the interpratation of the different data, ranging from structural and material inspection to biological and physical phenomena. The 3D approach is particularly useful in the case under investigation, where the projections are a given by a set of digital camera pictures, which will be considered as the discrete 3D Radon transforms of the visible light emission. We develop an algorithm of image reconstruction and apply it to the 3D reconstruction of the light emission density of magnetically confined Helium and Hydrogen plasma. Data was recorded during the deployment of the PROTO-SHPERA experiment [2], which took place at ENEA (Italian National Agency for New Technologies, Energy and Sustainable Development) laboratories in Frascati, Italy. During the experiment, the plasma emits photons, which light is captured by six cameras arranged with cylindrical symmetry. The PROTO-SHPERA experiment is an innovative magnetic confinement plasma experiment for controlled thermonuclear fusion research, whose aim is to form a plasma torus not around a metal centerpost, as in tokamaks, but around a plasma centerpost.

This paper is organized into two sections: Section 2 describes the proposed method for image reconstruction, and Section 3 reports the experimental results. In Subection 2.1, the 3D continuous Radon transform is recalled, then in Subsection 2.2 the lemma of the Fourier slice theorem that is at the base of the image reconstruction method employed is proved. In Subsection 2.3 proof of the effectiveness of the reconstruction method is provided by using numerical data. Subection 3.1 describes the PROTO-SPHERA experiments, and Subsecion 3.2 illustrates how the tomographic reconstruction enabled to prove the sustainment of the plasma torus around the centerpost and provided further useful information on the dynamics of confined plasma.

2. Analytical direct 3D image reconstruction

2.1. 3D continuous Radon Transform

For simplicity's sake, the 2D Radon transform is first introduced. Let us consider a plane object - or a slice of a 3D object - with density function $f(x, y)$ (Figure 1). Its projections onto a line inclined by an angle θ with respect to the x axis are obtained by integrating $f(x, y)$ on the set of parallel lines (rays) that are inclined by an angle $\theta + \pi/2$ with respect to the x axis and at a distance t from the origin of the coordinate system (bold line in 1). The equation of a ray is:

$$t = x\,cos\theta + y\,sin\theta. \tag{1}$$

The projection of the function $f(x, y)$ is then defined as:

$$p(\theta, t) = \int_{-\infty}^{\infty}\int_{-\infty}^{\infty} f(x, y)\delta(x\,cos\theta + y\,sin\theta - t)dxdy, \tag{2}$$

where δ is the Dirac's delta function. Equation (2) represents the 2D continuous Radon transform $[\mathcal{R}_2 f](\theta, t)$ of the function f, which is depicted schematically in Figure 1 by the blue curve subtending the sky blue area. It is often preferred to integrate in the rotated coordinate system (t, s), where the projection can be written as:

$$p(\theta, t) = \int_{-\infty}^{\infty} f(t, s)ds. \tag{3}$$

Geometrically, the continuous 2D Radon transform maps a function in $\mathbb{R}^2$ into the set of its line integrals in $\mathbb{R}^2$. The reconstructed image function $f(x, y)$ is formally obtained by inverting the Radon transform:

$$f(x, y) = [\mathcal{R}_2^{-1} p](\theta, t). \tag{4}$$

Let us now consider a 3D object with density function $f(x, y, z)$ (Figure 2). Its projections are obtained by integrating $f(x, y, z)$ on the plane Σ that is orthogonal to the versor $\boldsymbol{\alpha}$ and at a distance d from the origin of the coordinate system. The versor has direction cosines $\boldsymbol{\alpha} = (cos\theta\, cos\phi, sin\theta\, cos\phi, sin\, \phi)^T$, where ϕ is the angle that $\boldsymbol{\alpha}$ forms with the z axis, and θ is the angle that the projection of $\boldsymbol{\alpha}$ onto the xy plane forms with the x axis. The equation of a plane orthogonal to $\boldsymbol{\alpha}$ and at a distance d from the origin is:

$$d = x\, cos\theta\, cos\phi + y\, sin\theta\, cos\phi + z\, sin\phi. \tag{5}$$

In an analogy with Equation (2), the projection of the function $f(x, y, z)$ associated with the couple $(\boldsymbol{\alpha}, d)$ is then defined as:

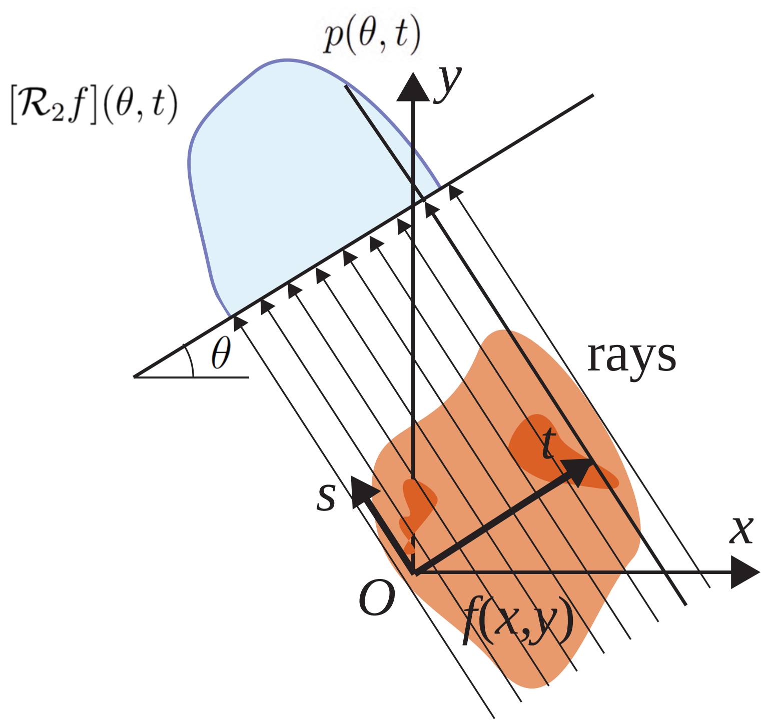

Figure 1: Projection of a plane density function onto a line.

$$p(\boldsymbol{\alpha}, d) = \int_{-\infty}^{\infty}\int_{-\infty}^{\infty}\int_{-\infty}^{\infty} f(x, y, z)\delta(x\, cos\theta\, cos\phi + y\, cos\theta\, sin\phi + z\, sin\theta - d) dxdydz. \tag{6}$$

The area over which the previous integral is computed is included in the dashed curve in Figure 2. Equation (6) represents the 3D continuous Radon transform $[\mathcal{R}_3 f](\boldsymbol{\alpha}, t)$ of the function f. Geometrically, the continuous 3D Radon transform maps a function in $\mathbb{R}^3$ into the set of its plane integrals in $\mathbb{R}^3$. The reconstructed image function $f(x, y, z)$ is formally obtained by inverting the Radon transform:

$$f(x, y, z) = [\mathcal{R}_3^{-1} p](\boldsymbol{\alpha}, d). \tag{7}$$

It is important to note that in real applications we won't be dealing with plane integrals. In fact, $\mathcal{R}_3$ can be obtained by computing the $\mathcal{R}_2$ of the intersection

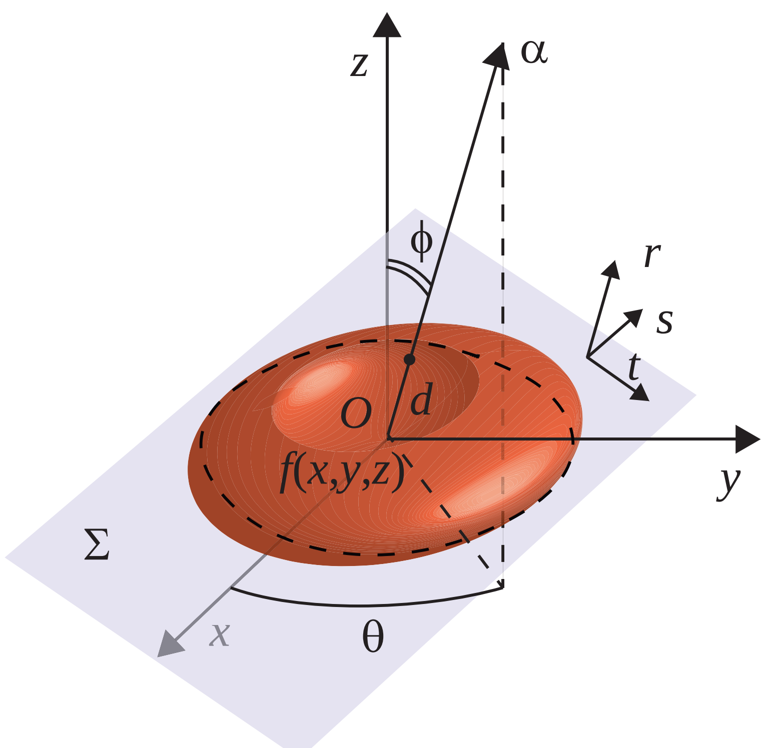

Figure 2: Projection of a 3D density function onto a plane.

between f and the plane Σ, and then integrating over lines orthogonal to the rays, which are displayed in Figure 3 as yellow lines. The line integrals are much easier to be obtained in practical measurements. They correspond to X-ray projections taken from different angles, or, in the present case, to pictures taken from different cameras.

Let us assume that the integration is carried out in the rotated coordinate system (t, s, r), whose axes t and s coincide with the tangent lines to the parallels and meridians, respectively, of an imaginary sphere centered in the origin of the system of coordinates, at the point of intersection between the sphere and the versor $\boldsymbol{\alpha}$, with the orientation of the r axis coinciding with that of $\boldsymbol{\alpha}$ (Figure 3, upper left). The transformation of coordinates from (x, y, z) to (t, s, r) can be written as:

$$\begin{bmatrix} t \\ s \\ r \end{bmatrix} = \begin{bmatrix} cos\phi & 0 & sin\phi \\ 0 & 1 & 0 \\ sin\phi & 0 & cos\phi \end{bmatrix} \begin{bmatrix} cos\theta & sin\theta & 0 \\ -sin\theta & cos\theta & 0 \\ 0 & 0 & 1 \end{bmatrix} \begin{bmatrix} x \\ y \\ z \end{bmatrix} \tag{8}$$

Moreover, the distance d can be expressend in the (t, s, r) system of coordinates as $d = \sqrt{t^2 + r^2}$. The ray integral is then expressed as follows:

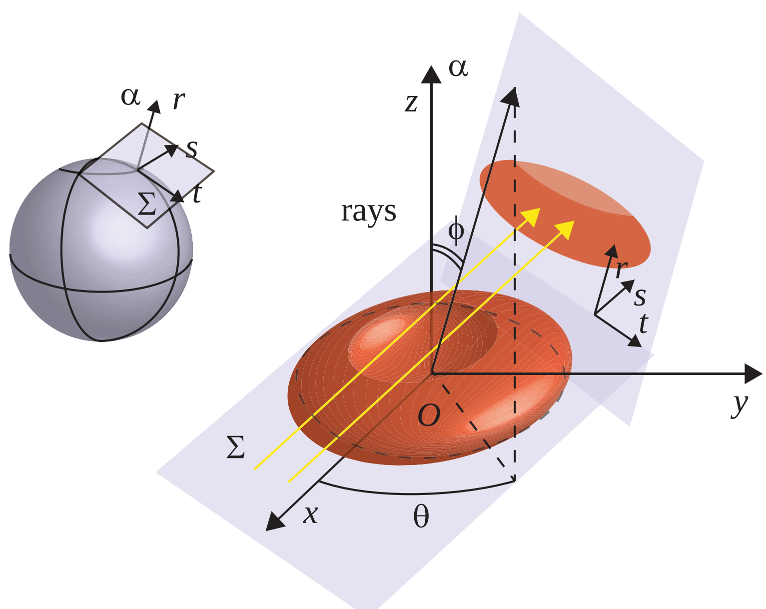

Figure 3: Ray integrals over a 3D function.

$$p(\theta, \phi, t, r) = \int_{-\infty}^{\infty} f(t, s, r) ds. \tag{9}$$

The integral $p(\theta, \phi, t, r)$ is in practice a line projection of the 3D function. The set of all the line projections on the plane (t, r) for given θ and ϕ will be denoted as $P_{\theta,\phi}$.

2.2. 3D Fourier slice theorem

The extension of the Fourier slice theorem to higher dimensions, enables direct reconstruction of 3D objects. The 3D Fourier Slice Theorem can be stated as follows.

Theorem 1. *A line slice of the 3D Fourier transform of the function $f(x, y, z)$ equals the 1D Fourier Transform of the 3D Radon transform $[\mathcal{R}_3 f](\boldsymbol{\alpha}, t)$ at the same angle.*

For proof, the interested reader can consult [38, 4]. However, the theorem in this form is of little use for practical purposes. A useful corollary can be stated.

Corollary 1.1. *A plane slice of the 3D Fourier transform of the density function $f(x, y, z)$ equals the 2D Fourier Transform of the set of line projections at the same angle.*

Proof. Let us consider the line projection of a 3D density function $P_{\theta,\phi}$, and take its 2D Fourier Transform ($\mathcal{F}_2$):

$$[\mathcal{F}_2 P_{\theta,\phi}](\mu, \nu) = \int_{-\infty}^{\infty} \int_{-\infty}^{\infty} P_{\theta,\phi}(t, r) e^{-2\pi i(\mu t + \nu r)} dt dr, \tag{10}$$

where μ and ν are the wavenumbers in the t, r directions, respectively and i is the imaginary unit.
By substituting equation (9) into equation (10), we get:

$$[\mathcal{F}_2 P_{\theta,\phi}](\mu, \nu) = \int_{-\infty}^{\infty} \int_{-\infty}^{\infty} [\int_{-\infty}^{\infty} f(t, s, r)) ds] e^{-2\pi i(\mu t + \nu r)} dt dr. \tag{11}$$

Based on the transformation (8), the rotated coordinate system (t, s, r) can be converted back into the initial (x, y, z) system:

$$[\mathcal{F}_2 P_{\theta,\phi}](\mu,\nu) = \int_{-\infty}^{\infty}\int_{-\infty}^{\infty}\int_{-\infty}^{\infty} f(x,y,z)e^{-2\pi i k}dxdydz \tag{12}$$

$$\text{with } k = \mu cos\phi\, cos\theta x + \mu cos\phi\, sin\theta y + \mu sin\phi z + \nu sin\phi\, cos\theta x + \\ + \nu sin\phi\, sin\theta y + \nu cos\phi\, z.$$

It is obvious that the right hand side of (12) represents the 3D Fourier Transform $\mathcal{F}_3$ of f at wavenumbers $u = \mu cos\phi\, cos\theta + \nu sin\phi\, cos\theta$, $v = \mu cos\phi\, sin\theta + \nu sin\phi\, sin\theta$ and $w = \mu sin\phi + \nu cos\phi$:

$$[\mathcal{F}_3 f](u,v,w) \int_{-\infty}^{\infty}\int_{-\infty}^{\infty}\int_{-\infty}^{\infty} f(x,y,z)e^{-2\pi i(ux+vy+wz)}dxdydz, \tag{13}$$

which proves the corollary. The quantities u, v and w are wavenumbers in directions x, y and z, respectively. □

The interesting consequence of this corollary is that, given the line projections, on calculating their 2D Fourier Transform, and then, the inverse 3D Fourier Transform of the resulting set of 2D Fourier transforms, the original image is directly reconstructed. The following subsection provides numerical proof of the effectiveness of the procedure.

2.3. Numerical example of the 3D direct reconstruction

Let us consider an input density function modeled as a cube with a uniform density of 0.5, side length of 0.6, and centered at the origin of the coordinate system (Figure 4a). Inside this cube, two smaller spheres are embedded: one with a density of 0.3, a radius of 0.1, and centered at coordinates (0.05, 0.05, -0.2); the other with a density of 0.1, a radius of 0.05, and centered at (-0.1, 0, 0.1). These variations in density are used to verify the accuracy of the reconstruction method, ensuring it can effectively distinguish between different density regions. Although the spheres are not visible from the exterior of the solid cube, Figure 4b illustrates their positions by rendering the cube with partial transparency. It is important to note that for this numerical example, the theoretical framework developed for continuous systems in the previous sections has been adapted for use with discrete data. In this case, we employed a total of $N = 64 \times 64 \times 64$ sampling points, with 64 points along each side of the cube. Additionally, $N_{deg} = 12 \times 12 = 144$ spherical projections were taken, with 12 projections for each angle θ and ϕ. The angular step size was kept constant over π, set to $\pi/12$.

Figures 5a and b provide samples of the spherical projections used for reconstruction, taken at angles $(\theta, \phi) = (\pi/2, 0)$ and $(2\pi/3, 0)$, respectively. Note that the color scale extends beyond 0.5 because it represents line integrals of the density function over the entire domain, rather than local values. Regions of lower density show in fact lower integral values. By combining a total of 144 two-dimensional Fourier transforms of the spherical projections and computing their three-dimensional inverse Fourier transform, the reconstructed density function shown in Figure 6a is obtained, matching the original function from Figure 4a. Figures 6b, c, and d present cross-sections of the reconstructed density function along two vertical planes (b,c) and a horizontal plane (d) passing through the origin, with the corresponding color scale. This Figure shows that the embeddes spheres are exacly reproduced not only in terms of position, but also in terms of density. See in fact that the large sphere has high density, while the small one low.

The previous example was implemented using a large number of projections. While reducing the number of projections results in a slightly blurred reconstructed image, even a very limited number of projections still provides a sufficiently clear reconstruction. This effect is illustrated in Figure 7, which shows the reconstructed density function with varying numbers of projections. The source density function is depicted in Figure 7. It is shaped as a cube with a unit density, a side length of 0.2, and is centered at the origin of the coordinate system. A sphere with unit density, a diameter larger than the cube's side, and centered at the origin, was subtracted from the density function, causing its volume to intersect with the cube's faces. Although the image quality decreases as the number of projections is reduced, the shape remains distinctly recognizable even with a very limited number of projections, as few as 9 (Figure 7d).

3. 3D Reconstruction of light emission density in PROTO-SPHERA experiment

3.1. The PROTO-SPHERA experiment

PROTO-SPHERA (Spherical Plasma for Helicity Relaxation Assessment) is an innovative magnetic confinement plasma experiment aimed at advancing controlled thermonuclear fusion research. Its goal is to form plasma within a confined environment. Unlike tokamaks, where the plasma forms around a metal centerpost, in PROTO-SPHERA, the plasma forms around a plasma centerpost [23]. Tokamaks, the most extensively studied magnetic

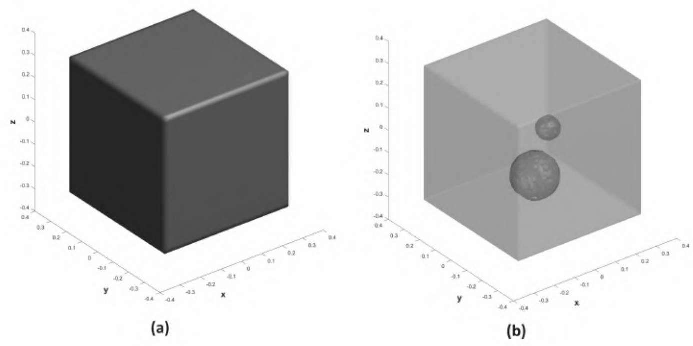

Figure 4: a) 3D density function b) density function made partially transparent to show the embedded spheres.

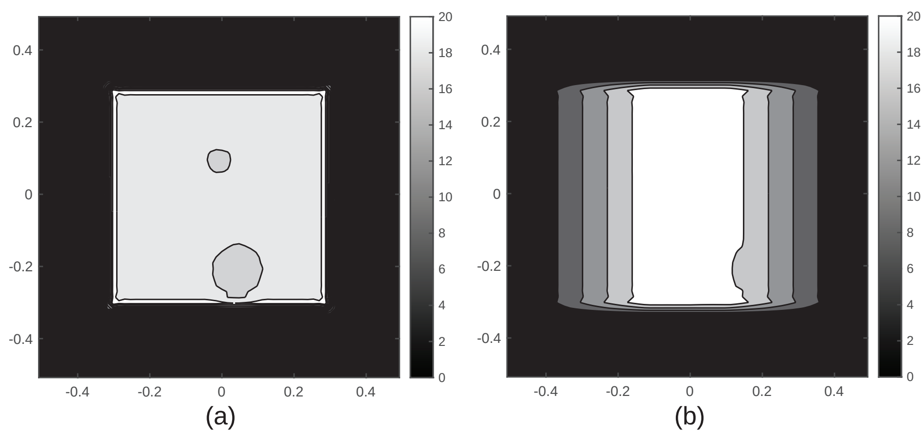

Figure 5: A couple of spherical projections pertaining to angles a) $\theta = \pi/2$, $\phi = 0$ and b) $\theta = 2\pi/3$, $\phi = 0$

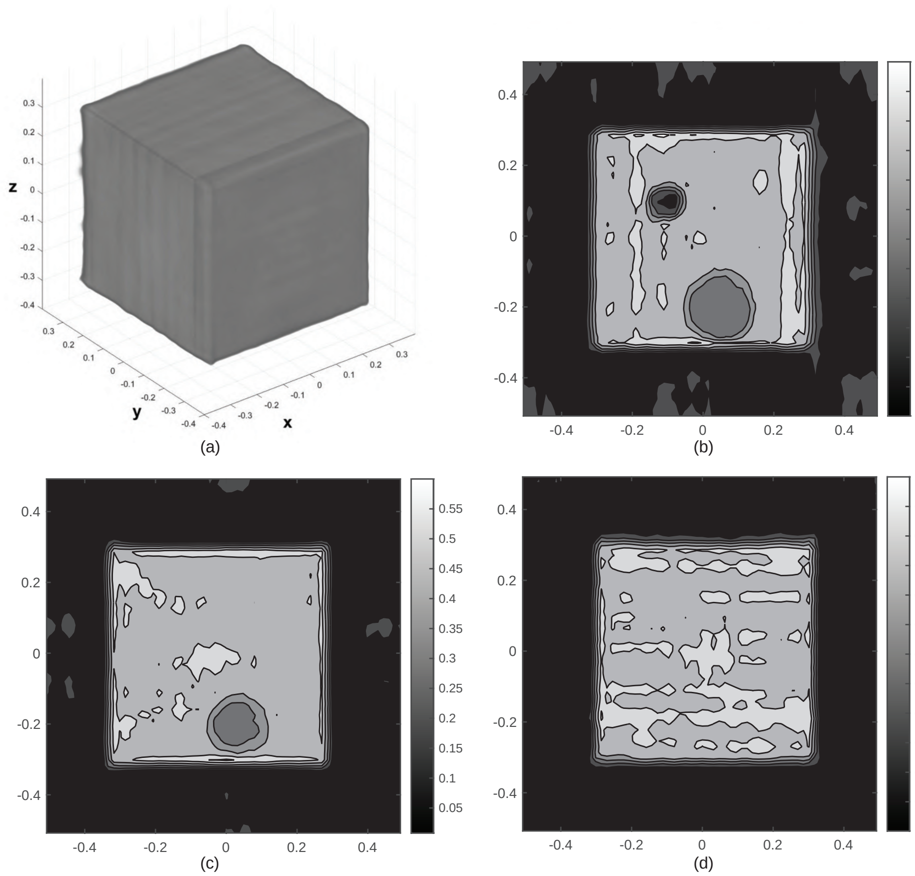

Figure 6: a) Reconstructed image, b) vertical cross section on the xz plane, c) vertical cross section on the yz plane, d) horizontal cross section on the xy plane.

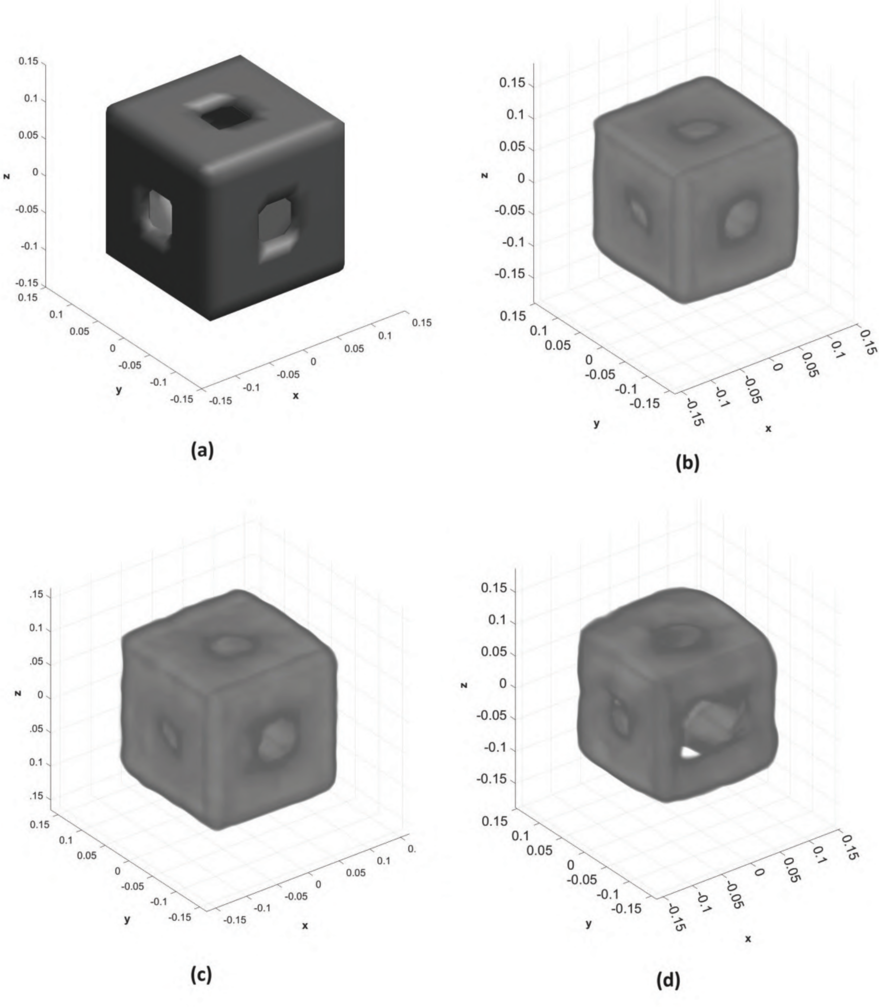

Figure 7: a) Source image and Reconstructed image with b) $12\times$, c) 6×6 and d) 3×3 projections.

fusion configurations, have a non-simply connected geometry, where a central post—containing the inner part of the toroidal magnet and the ohmic transformer—connects the plasma torus. The development of simply connected magnetic configurations relevant for fusion would significantly simplify the design of fusion reactors. Additionally, the PROTO-SPHERA experiment seeks to emulate astrophysical plasmas, such as jet and torus structures, in a laboratory setting [2].

Figure 8 shows a schematic of the PROTO-SPHERA experiment, which consists of a transparent cylindrical vacuum chamber measuring 2.5 meters in height and 2.0 meters in diameter. The chamber is equipped with electrodes at the ends and internal poloidal field coils. The operating sequence proceeds as follows: the tungsten filaments of the cathode are heated to 2600°C over 30 seconds, while the current in the poloidal field coils is ramped up to 1875 A. Gas is then introduced through a hollow section in the anode, reaching a pressure of 10^{-2} to 10^{-1} mbar, and a total voltage of 100-350 V is applied between the electrodes. Under these conditions, plasma forms and emits photons.

To study the plasma formation process and the magneto-hydrodynamic phenomena occurring in the experiment, six high-speed cameras are positioned on the equatorial plane of the chamber, spaced 60 degrees apart (Figure 9). Each camera has a resolution of 640x480 pixels and can capture 600 frames per second. Sample images recorded by the cameras at a specific time instant are shown in Figures 10a and 11a for shots with Helium and Hydrogen, respectively.

Combining the data from the cameras with measurements from a Langmuir probe has provided valuable insights into the dynamics of the plasma torus formation, including its size and emission spectrum. Numerous discharges were produced and observed throughout the experimental campaign.

The images captured by the six cameras are in fact projections onto planes of the visibile-light emission density, which plays the role of the density function f (Figures 10a and 11a). For each time instant, exploiting the corollary of the Fourier Slice Theorem of Section 2, these source images are 2D-Fourier transformed, then 3D-Fourier inverted to obtain the density of the visible light emitted by the plasma. The only change with respect to the procedure described in Section 2.2 is that, given the positioning of the cameras, the inversion has to be based on a cylindrical set of parallel projections instead of a spherical set, with ϕ fixed. Figures 10b and 11b show the reconstructed plasma light emission distribution derived from the images on the left. It is important to note that the original images contain three layers of information, corresponding to the RGB color channels. The reconstructed images in Figures 10b and 11b are false-color representations, created by combining the RGB channels linearly with the following weighting: 100% Red, 86% Green, and 25% Blue [2].

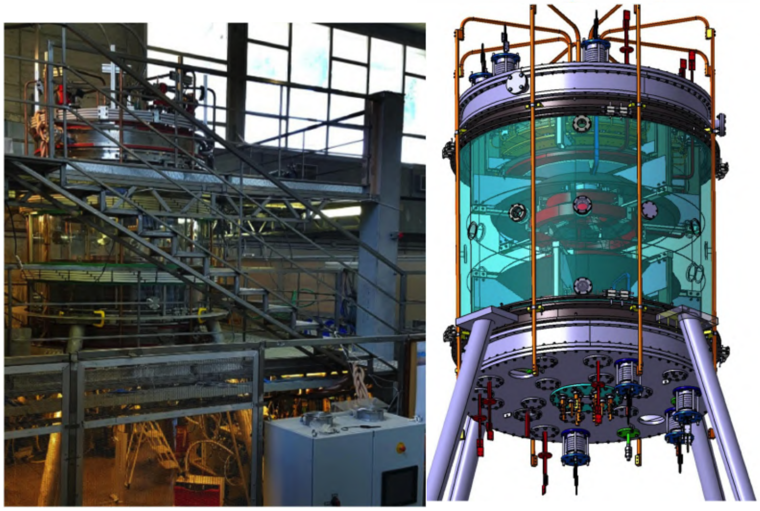

Figure 8: Schematic of the PROTO-SPHERA experiment

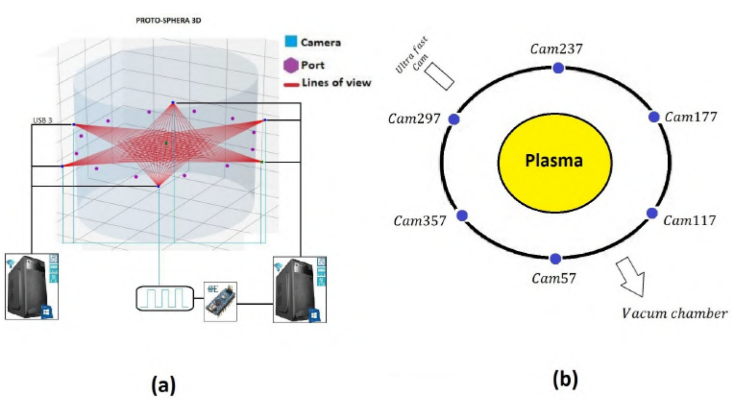

Figure 9: a) Position of the cameras in axonometry b) and plan

3.2. Results and discussion

The proposed 3D tomography technique enabled detailed observation of the plasma torus formation process. According to magneto-hydrodynamic models [14], the sequence begins with the formation of a plasma column (pinch or centerpost) at low current. As the current increases, the magnetic field lines bend, causing the pinch to become unstable, which leads to the formation of a torus around the centerpost. This progression is visualized in Figure 12 a-h, showing the reconstructed light emission density at eight sequential time steps (each 1/600 s apart) during a Helium plasma discharge. The same sequence predicted by the work of García-Martínez et al. [14] is observed. The entire torus formation occurs within approximately 8 ms, five time steps intercurring from the arrangements of Figure 12 b to g. The presence of both jets and the torus strongly parallels astrophysical phenomena, as discussed in [2].

Once the spatial distribution of light emission density is known for each time instant, cross-sections can be derived, revealing further insights into plasma dynamics. Figure 13 shows an image of the Helium plasma captured by one of the six cameras (a) and a vertical cross-section (b) of the reconstructed light emission density in true color, taken at the same moment. To create this image, each of the three RGB channels was processed independently to generate a corresponding density function for each color. This cross-sectional view reveals the green color, which was obscured in the camera pictures by the intense golden glow of the 'ionization peel'—the layer between the plasma and the surrounding gas cushion. The correcness of the reconstruction is proved by the appearance of the Langmiur probe and of the copper bars on the right hand side of the picture.

Figure 14 presents vertical cross-sections of the plasma light emission density at the same time instants as Figure 12. These images further confirm the sequence of events leading to the formation of the torus, as described in the previous paragraph. Specifically, Figure 14 illustrates the emergence of a stable pinch (a-b), its progression towards instability (c-f), and ultimately the arrangement of the torus around the centerpost (d-h). Similar patterns, with comparable duration, were observed in other plasma discharges [2, 28]. Figure 15 presents a horizontal cross-section at the equatorial level, enabling observation of the same phenomena from a different perspective. In Figures 15d and 15e, the pinch's instability is particularly evident, as shown by the loss of axial symmetry and the presence of green regions on the right side of the images. Additionally, the horizontal cross-section analysis provides insights into plasma stability and torus thickness. Figure 16 illustrates selected horizontal cross-sections of Helium plasma at the equatorial level across sequential times, clearly depicting the torus encircling the centerpost. Notably, the light emission intensity varies over time, suggesting potential correlations with plasma density and stability. These images also allowed for the measurement of torus thickness, defined as the difference between the outer and inner circumferences' radii, which was observed to be between 0.25 and 0.35 m. Similar behaviors were noted for Hydrogen plasma discharges, with an equatorial horizontal cross-section provided in Figure 17 for reference.

4. Conclusions

An imaging technique based on the formulation of a corollary the Fourier slice theorem was applied to reconstruct the light emission distribution of magnetically confined plasma in three dimensions. The algorithm was used on data capturing the visible light emission from Helium and Hydrogen plasmas, recorded by six cameras as part of the PROTO-SPHERA experiment at the ENEA Frascati laboratories. The results demonstrate that six images taken by cameras arranged in cylindrical symmetry enable an accurate 3D reconstruction of the plasma's spatial distribution at different time instants during the experiment. We observed that the plasma torus forms in approximately 8 ms, evolving from a kinked filament caused by the destabilization of the plasma centerpost. This 3D reconstruction allows for cross-sectional analysis, revealing previously hidden green light emission from the core, which had been obscured by the outer golden ionized layer. Additionally, equatorial cross-sections enabled the measurement of the torus thickness, which was found to range between 0.25 and 0.35 meters.

5. Acknowledgement

Annamaria Pau gratefully acknowledges the funding contribution from National Center on HPC, Big Data and Quantum Computing CN00000013. This manuscript reflects only the authors' views and opinions, neither the European Union nor the European Commission can be considered responsible for them.

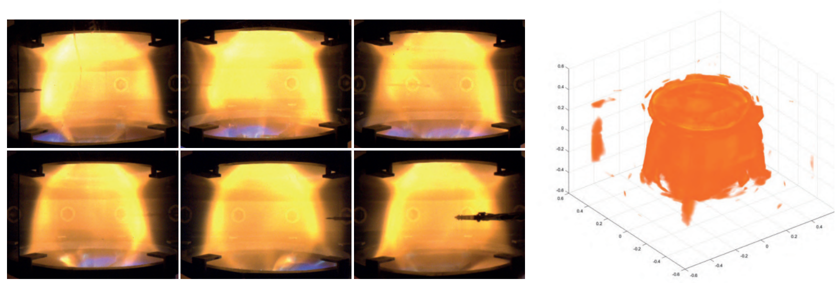

(a) (b)

Figure 10: a) Pictures recorded by the six cameras at a given time instant (267 msec) of the PROTO-SPHERA experiment from shot 2505 of Helium b) 3D reconstruction of plasma light emission density

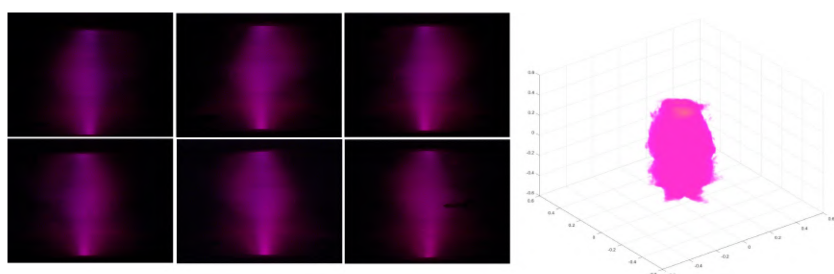

(a) (b)

Figure 11: a) Pictures recorded by the six cameras at a given time instant (233msec) of the PROTO-SPHERA experiment from shot 2154 of Hydrogen b) 3D reconstruction of plasma light emission density

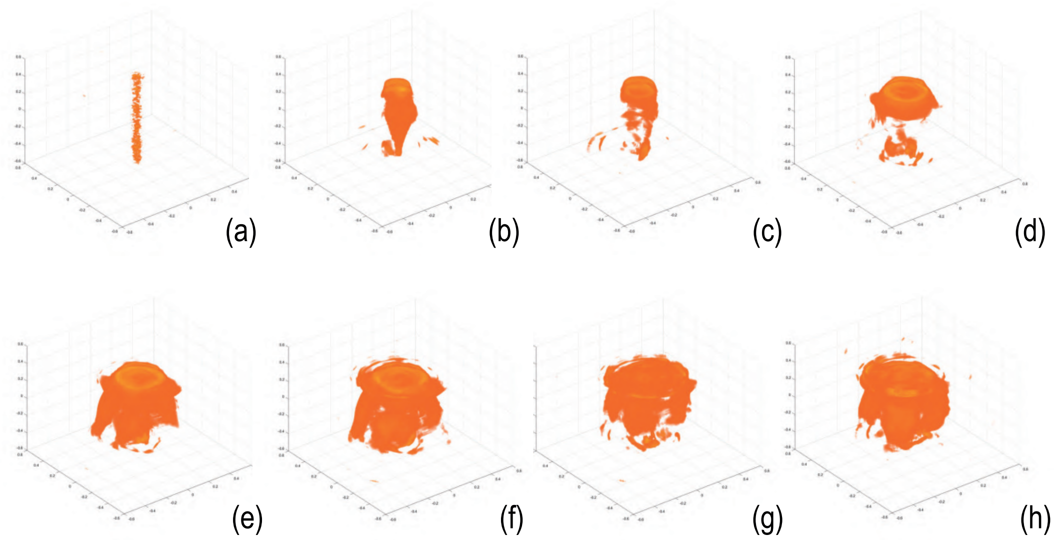

Figure 12: Reconstructed light emission density of Helium discharge 2505 at eight sequential time steps: stable pinch (a-b), pinch instability (c-f), formation of the plasma torus around the pintch (g-h)

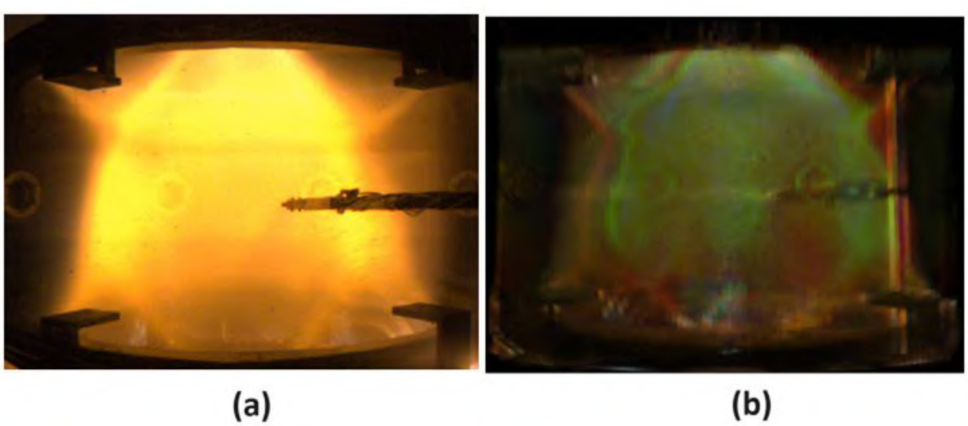

Figure 13: A projection of Helium plasma visible light emission captured by a camera during shot 2141 (a) and cross-section of the reconstructed light emission density in true colors (b).

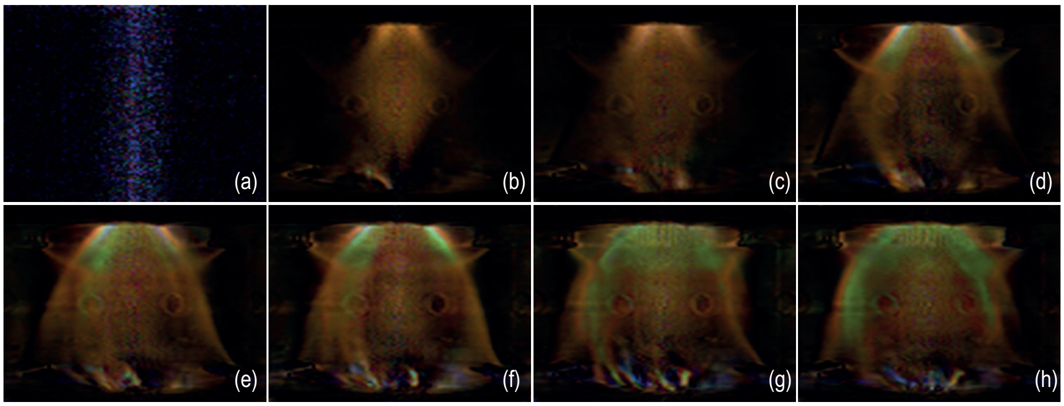

Figure 14: Vertical cross-sections of the reconstructed light emission density of Helium discharge 2505 at the same eight sequential time instants as Figure 12: stable pinch (a-b), pinch instability (c-f), formation of the plasma torus around the pinch (g-h)

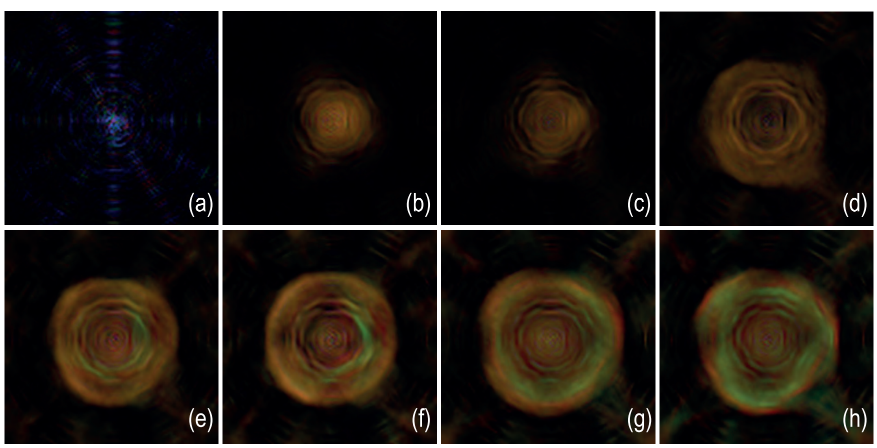

Figure 15: Horizontal cross-sections of the reconstructed light emission density of Helium discharge 2505 at the same eight sequential time instants as Figure 12: stable pinch (a-b), pinch instability (c-f), formation of the plasma torus around the pinch (g-h)

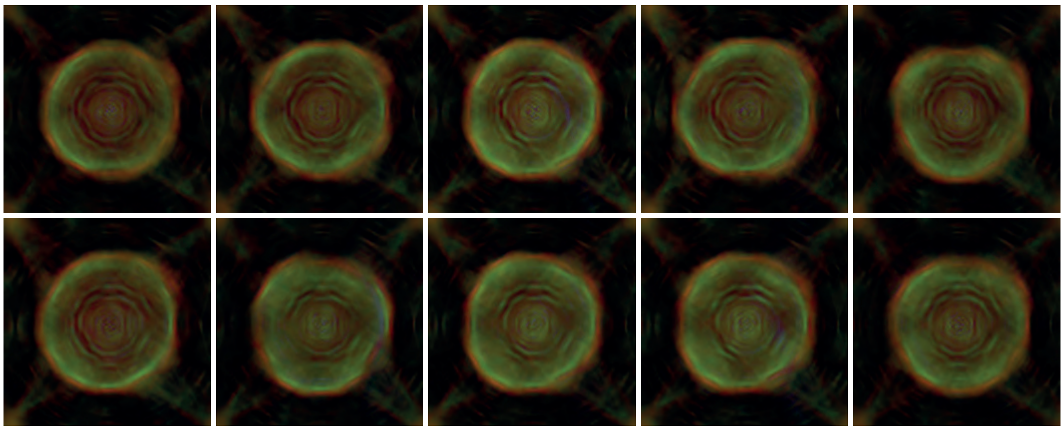

Figure 16: Sequence of reconstructed equatorial cross-sections of light emission density of Helium discharge 2505 at 10 time instants

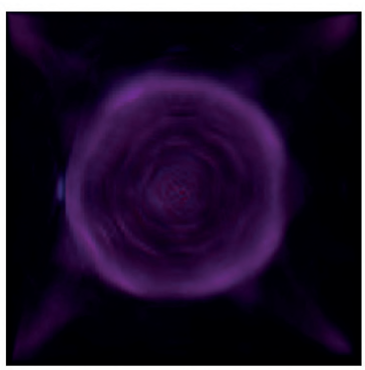

Figure 17: Equatorial cross-section of light emission density of Helium discharge 2154

References

[1] Amir M. Alani, Francesco Soldovieri, Ilaria Catapano, Iraklis Giannakis, Gianluca Gennarelli, Livia Lantini, Giovanni Ludeno, and Fabio Tosti. The use of ground penetrating radar and microwave tomography for the detection of decay and cavities in tree trunks. *Remote Sensing*, 11(18), 2019.

[2] F. Alladio, P. Micozzi, L. Boncagni, A. Pau, S. Naghinajad, S. Macera, Y. Damizia, P. Buratti, F. Filippi, G. Galatola Teka, F. Giammanco, E. Giovannozzi, M. Iafrati, A. Lampasi, and P. Marsili. PROTO-SPHERA: a magnetic confinement experiment which emulates the jet + torus astrophysical plasmas. *Plasma Physics and Controlled Fusion*, 66(3), 2024.

[3] Habib Ammari. Tomographic imaging with non-diffracting sources. an introduction. *Mathematics of Emerging Biomedical Imaging*, 28(10):95–106, 2008.

[4] Amir Averbuch and Yoel Shkolnisky. 3d Fourier based discrete Radon transform. *Applied and Computational Harmonic Analysis*, 15(1):33 – 69, 2003.

[5] V. Cnudde and M.N. Boone. High-resolution X-ray computed tomography in geosciences: A review of the current technology and applications. *Earth-Science Reviews*, 123:1 – 17, 2013.

[6] A. M. Cormack. Early two-dimensional reconstruction and recent topics stemming from it. *Science*, 209:1482–1486, 1980.

[7] Petras Daras, Dimitrios Zarpalas, Dimitrios Tzovaras, and Michael G. Strintzis. Shape matching using the 3d Radon transform. page 953 – 960, 2004.

[8] L. De Chiffre, S. Carmignato, J.-P. Kruth, R. Schmitt, and A. Weckenmann. Industrial applications of computed tomography. *CIRP Annals - Manufacturing Technology*, 63(2):655 – 677, 2014.

[9] S.R. Deans. *The Radon Transform and some of its applications*. Wiley: New York, 1983.

[10] Musa Sani Musa Niyazi Şentürk Fatih Veysel Nurçin Dilber Uzun Ozsahin, Berna Uzun and Ilker Ozsahin. Evaluating nuclear medicine imaging devices using fuzzy PROMETHEE method. *Procedia computer science*, 120:699–705, 2017.

[11] S. Donato, L. Brombal, L.M. Arana Peña, F. Arfelli, A. Contillo, P. Delogu, F. Di Lillo, V. Di Trapani, V. Fanti, R. Longo, P. Oliva, L. Rigon, L. Stori, G. Tromba, and B. Golosio. Optimization of a customized simultaneous algebraic reconstruction technique algorithm for phase-contrast breast computed tomography. *Physics in Medicine and Biology*, 67(9), 2022.

[12] Mario D'Acunto, Antonio Benassi, Davide Moroni, and Ovidio Salvetti. 3D image reconstruction using Radon transform. *Signal, Image and Video Processing*, 10(1):1 – 8, 2016.

[13] Jeffrey Fessler. Optimization methods for magnetic resonance image reconstruction: Key models and optimization algorithms. *IEEE signal processing magazine*, 37(1):33–40, 2020.

[14] Pablo Luis García-Martínez, Leandro Gabriel Lampugnani, and Ricardo Farengo. Effect of the helicity injection rate and the Lundquist number on spheromak sustainment. *Physics of Plasmas*, 21(12), 2014.

[15] Richard Gordon, Robert Bender, and Gabor T. Herman. Algebraic reconstruction techniques (ART) for three-dimensional electron microscopy and x-ray photography. *Journal of Theoretical Biology*, 29(3):471–476,IN1–IN2,477–481, 1970.

[16] David Gottlieb, Bertil Gustaffson, and Patrick Forssen. On the direct Fourier method for computed tomography. *IEEE Transactions on Medical Imaging*, 19(3):223–232, 2000.

[17] B Gustaffson. Mathematics for computed tomography. *Physica Scripta*, T61:38– 43, 1996.

[18] G. N. Hounsfield. Computerized transverse axial scanning (tomography): Part I. description of system. *British Journal of Radiology*, 46(3):1016–1022, 1973.

[19] P. Huthwaite. Guided wave tomography with an improved scattering model. *Proceedings of the Royal Society A: Mathematical, Physical and Eng. Sciences*, 472(2195), 2016.

[20] A. C. Kak and M. Slaney. *Principles of Computerized Tomographic Imaging*. IEEE press, 1988.

[21] Avinash C. Kak. Computerized tomography with X-ray, emission, and ultrasound sources. *Proceedings of the IEEE*, 67(9):1245 – 1272, 1979.

[22] Mohd Taufiq Mohd Khairi, Sallehuddin Ibrahim, Mohd Amri Md Yunus, M. Faramarzi, Goh Pei Sean, Jaysuman Pusppanathan, and A. Abid. Ultrasound computed tomography for material inspection: Principles, design and applications. *Measurement: Journal of the International Measurement Confederation*, 146:490 – 523, 2019.

[23] Alessandro Lampasi, Giuseppe Maffia, Franco Alladio, Luca Boncagni, Federica Causa, Edmondo Giovannozzi, Luigi Andrea Grosso, Alessandro Mancuso, Paolo Micozzi, Valerio Piergotti, Giuliano Rocchi, Alessandro Sibio, Benedetto Tilia, and Vincenzo Zanza. Progress of the plasma centerpost for the PROTO-SPHERA spherical tokamak. *Energies*, 9(7), 2016.

[24] Xin Li, Yudong Lu, Xiaozhou Zhang, Wen Fan, Yangchun Lu, and Wangsheng Pan. Quantification of macropores of malan loess and the hydraulic significance on slope stability by x-ray computed tomography. *Environmental Earth Sciences*, 78(16), 2019.

[25] E. Maire and P.J. Withers. Quantitative X-ray tomography. *Int. Materials Reviews*, 59(1):1 – 43, 2014.

[26] Tugba Ozge Onur. An application of filtered back projection method for computed tomography images. *International Review of Applied Sciences and Engineering*, 12(2):194 – 200, 2021.

[27] Yongwoo Park, Un-Chul Paek, and Dug Young Kim. Characterization of a stress-applied polarization-maintaining (PM) fiberthrough photoelastic tomography. *Journal of lightwave technology*, 21(4):997 – 1004, 2003.

[28] A. Pau, S. Naghinajad, F. Alladio, P. Micozzi, and L. Boncagni. 3D tomography of Hydrogen and Helium plasma produced in th PROTO-SPHERA experiment. In *Proceedings of the ASME 2024 51st Annual Review Progress in Quantitative Nondestructive Evaluation QNDE2024*, pages 1–7, Denver, Colorado, July 2024.

[29] Johann Radon. On the determination of functions from their integral values along certain manifolds (translation from the original German text published in Berichte der Sächsischen Akademie der Wissenschaft, vol. 69, pp. 262-277, 1917). *IEEE Transactions on Medical Imaging*, MI-5(4):170–176, 1986.

[30] L. Schoeman, P. Williams, A. du Plessis, and M. Manley. X-ray micro-computed tomography (μCT) for non-destructive characterisation of food microstructure. *Trends in Food Science and Technology*, 47:10 – 24, 2016.

[31] James Anthony Seibert. Iterative reconstruction: how it works, how to apply it. *Pediatric Radiology*, 44(3):431 – 439, 2014.

[32] Wolfram Stiller. Basics of iterative reconstruction methods in computed tomography: A vendor-independent overview. *European Journal of Radiology*, 109:147 – 154, 2018.

[33] Weijie Tao, Damien Rohmer, Grant T. Gullberg, Youngho Seo, and Qiu Huang. An analytical algorithm for tensor tomography from projections acquired about three axes. *IEEE Transactions on Medical Imaging*, 41(11):3454 – 3472, 2022.

[34] M. Vassholz, B. Koberstein-Schwarz, A. Ruhlandt, M. Krenkel, and T. Salditt. New x-ray tomography method based on the 3d Radon transform compatible with anisotropic sources. *Physical Review Letters*, 116(8), 2016.

[35] M.L.L. Wijerathne, Kenji Oguni, and Muneo Hori. Tensor field tomography based on 3D photoelasticity. *Mechanics of Materials*, 34(9):533 – 545, 2002.

[36] Tao Zhang, Yuxiang Xing, Li Zhang, Xin Jin, Hewei Gao, and Zhiqiang Chen. Stationary computed tomography with source and detector in lin-

ear symmetric geometry: Direct filtered backprojection reconstruction. *Medical physics*, 47(5):2222–2236, 2020.

[37] Yingying Zhang-O'Connor and Jeffrey A. Fessler. Fourier-based forward and back-projectors in iterative fan-beam tomographic image reconstruction. *IEEE Transactions on Medical Imaging*, 25(5):582 – 589, 2006.

[38] Dominique Zosso, Benoît Le Callennec, Meritxell Bach Cuadra, Kamiar Aminian, Brigitte M. Jolles, and Jean-Philippe Thiran. Bi-planar 2d-to-3d registration in fourier domain for stereoscopic x-ray motion tracking. volume 6914, 2008.